



Core/shell rGO/BiOBr particles with visible photocatalytic activity towards water pollutants

Lakhdar Allagui, Bilel Chouchene, Thomas Gries, Ghouti Medjahdi, Emilien Girot, Xavier Framboisier, Abdesslem Ben Haj Amara, Balan Lavinia, Lavinia Balan, Raphael Schneider

► To cite this version:

Lakhdar Allagui, Bilel Chouchene, Thomas Gries, Ghouti Medjahdi, Emilien Girot, et al.. Core/shell rGO/BiOBr particles with visible photocatalytic activity towards water pollutants. *Applied Surface Science*, 2019, 490, pp.580-591. 10.1016/j.apsusc.2019.06.091 . hal-03088840

HAL Id: hal-03088840

<https://hal.science/hal-03088840v1>

Submitted on 27 Dec 2020

HAL is a multi-disciplinary open access archive for the deposit and dissemination of scientific research documents, whether they are published or not. The documents may come from teaching and research institutions in France or abroad, or from public or private research centers.

L'archive ouverte pluridisciplinaire **HAL**, est destinée au dépôt et à la diffusion de documents scientifiques de niveau recherche, publiés ou non, émanant des établissements d'enseignement et de recherche français ou étrangers, des laboratoires publics ou privés.

Core/shell rGO/BiOBr particles with visible photocatalytic activity towards water pollutants

Lakhdar Allagui,^a Bilel Chouchene,^b Thomas Gries,^c Ghouti Medjahdi,^c Emilien Girot,^b Xavier Framboisier,^b Abdesslem Ben haj Amara,^a Lavinia Balan,^d Raphaël Schneider^{b*}

^a Laboratoire de Physique des Matériaux Lamellaires et Nano-Matériaux Hybrides, Faculté des Sciences de Bizerte, Université de Carthage, 7021 Bizerte, Tunisie

^b Laboratoire Réactions et Génie des Procédés, Université de Lorraine, CNRS, F-54000 Nancy, France

^c Institut Jean Lamour, Université de Lorraine, CNRS, IJL, F-54000 Nancy, France

^d Institut de Science des Matériaux de Mulhouse, CNRS, UMR 7361, 15 rue Jean Starcky, 68093 Mulhouse, France

* Corresponding author : Tel. : +33 372743790

E-mail address : raphael.schneider@univ-lorraine.fr

Abstract

A series of heterostructured photocatalysts associating reduced graphene oxide (rGO) and BiOBr sheets with exposed {001} facets were prepared via a hydrothermal method. TEM experiments demonstrate that rGO deposits at the surface of BiOBr sheets to yield shell/core rGO/BiOBr particles. Under visible light irradiation, the rGO (1%)/BiOBr photocatalyst exhibits the highest activity for the degradation of the Orange II dye and for the removal of acetaminophen. This result originate from the increased visible light absorption and from the effective separation of charge carriers. Investigations into the photocatalytic mechanism show that holes in the valence band of BiOBr and superoxide $O_2^{\cdot -}$ radicals generated by the photocatalyst are the main species responsible for the oxidation of acetaminophen. The rGO (1%)/BiOBr catalyst was also demonstrated to be of high stability, further highlighting its potential for practical photocatalytic applications.

Keywords : BiOBr; Reduced graphene oxide; Photocatalyst; Charge separation

1. Introduction

In recent years, semiconductor photocatalysis has emerged as one of the most promising methods for energy conversion and environmental remediation [1-6]. When considering air and wastewater treatment, photogenerated electrons and holes react with oxygen and water molecules adsorbed at the surface of the photocatalyst to generate reactive species that are able to degrade pollutants into water, carbon dioxide and inorganic salts. Thus, the efficient absorption of visible light and the separation of photogenerated charge carriers constitute key elements to develop photocatalysts exhibiting a high efficiency.

Bismuth oxyhalides BiOX (X = Cl, Br or I) are emerging photocatalysts due to their stability, low toxicity and high photocatalytic efficiency. These materials exhibit a layered structure composed of $[Bi_2O_2]^{2+}$ slabs interleaved by double slabs of halogen ions [7-9]. The internal static electric field generated by this layered structure improves both the separation and the transfer of photogenerated electron-hole pairs along the (001) direction, which enhance the photocatalytic activity [10-12]. Thus, the development of BiOX photocatalysts with exposed {001} facets is a currently highly studied research topic [13-16]. Among bismuth oxyhalides, BiOBr is of high interest for photocatalytic applications. However, due to its relatively wide bandgap of 2.87 eV, BiOBr suffers from its modest visible-light photoresponse. Moreover, BiOBr exhibits a low surface adsorption ability [17].

Due to their good mechanical stability, excellent electron transport properties (up to 200000 $cm^2/V/s$) that enhance photoinduced charge transfer and to their high specific surface area ca. $2600 m^2/g$), graphene-based materials are co-catalysts of high interest for various photocatalytic applications ranging from water remediation to fuel production [18-28]. Moreover, graphene materials allow to extend the visible light absorption of photocatalysts. The development of new synthetic methodologies for the preparation of BiOBr-graphene composites has been the subject of numerous studies in recent years. Using graphene oxide (GO) or reduced graphene oxide (rGO), BiOBr spherical, plate-like or sheet-like particles associated or deposited at the surface of graphene sheets can be prepared via solvothermal, hydrothermal or precipitation methods [29-46]. The rGO/BiOBr composites were found to exhibit a high photocatalytic activity for the degradation of dyes (Methyl Orange, Methylene

Blue, Rhodamine), of aromatic derivatives (phenol, nitrobenzene) and for the removal of nitrogen monoxide (NO) [29-46].

In this paper, we report the successful association of BiOBr sheets possessing exposed {001} facets with rGO via a hydrothermal process using $\text{Bi}(\text{NO}_3)_3$ and KBr as precursors of BiOBr. Results show that rGO was found to deposit at the surface of BiOBr yielding rGO/BiOBr shell/core plate-like particles. The rGO (1%)/BiOBr composite exhibits a high photocatalytic activity under visible light irradiation in the photodegradation of the Orange II diazo dye but also for the removal of the acetaminophen drug from aqueous solutions.

2. Experimental section

2.1. Materials

Graphite powder (Merck), KMnO_4 (> 99%, Sigma), H_2O_2 (30%, VWR Chemicals), sodium nitrate (> 99%, Sigma), H_2SO_4 (reagent grade), L-ascorbic acid (reagent grade, Sigma), $\text{Bi}(\text{NO}_3)_3 \cdot 5\text{H}_2\text{O}$ (>99.99%, Sigma), KBr (>99%, Sigma), NaOH (> 97%, Sigma), and ethanol were used as received without further purification. All solutions were prepared using Milli-Q water ($18.2 \text{ M}\Omega \cdot \text{cm}$, Millipore) as solvent.

2.2. Synthesis of exfoliated graphene oxide

Graphite oxide was prepared by oxidation of graphite by a modified Hummer's method followed by an exfoliation [47]. Briefly, graphite (2 g) and NaNO_3 (1 g) were mixed in a flask cooled at 4°C using an ice bath. Then, concentrated H_2SO_4 (50 mL) was dropwise added to the flask and the mixture was stirred for 30 min. KMnO_4 (0.3 g) was then added and the mixture further stirred for 30 min. Next, KMnO_4 (7 g) was gradually added and the mixture further stirred for 1 h at a temperature below 20°C . The temperature was raised to 35°C and the solution was stirred for 2 h. Then, H_2O (90 mL) was slowly added (the temperature increased to 70°C) and the mixture stirred for 15 min, followed by the addition of mixture of 7 mL H_2O_2 and 55 mL of water to reduce the residual permanganate to soluble manganese ions. The resulting suspension was filtered, washed by centrifugation with 5% HCl (2500 rpm, 10 min, 4 times) followed by water (4000 rpm, 10 min, 5 times) and finally dried at 60°C for

24 h to obtain a brownish graphite oxide powder. The graphite oxide powder was dispersed in water (1 mg/mL) to obtain a suspension. Then, the suspension was ultra-sonicated for 1 h by probe sonication to obtain a graphene oxide suspension. Finally, the suspension was centrifuged at 5000 rpm for 15 min to collect graphene oxide (GO) pellets. The GO pellets were dried at 60°C for 24 h before use.

2.3. Synthesis of reduced graphene oxide

The reduction of GO into rGO was conducted according to the procedure described by Zhang et al. [48] with slight modifications. Briefly, GO (15 mg) was dispersed in 50 mL water at room temperature. L-Ascorbic acid (200 mg) was next added and the mixture stirred for 24 h under ambient conditions. rGO was recovered by centrifugation (4000 rpm for 15 min), washed with water, and dried overnight at 50°C.

2.4. Synthesis of BiOBr/rGO composites

Pure BiOBr was prepared according to reference [16]. rGO/BiOBr composites were prepared according to the following synthetic protocol. $\text{Bi}(\text{NO}_3)_3 \cdot 5\text{H}_2\text{O}$ (4 mmol) and rGO were dispersed under sonication in 36 mL of 1M HNO_3 . The loading in rGO was varied to prepare composites containing 0.5, 1, 2.5 and 5 wt% rGO relative to BiOBr. KBr (4 mmol) was dissolved into 12 mL of HNO_3 (1M). Then, the KBr solution was added dropwise to the $\text{Bi}(\text{NO}_3)_3$ -rGO mixture and the solution stirred for 30 min at room temperature. Next, the mixture was transferred into a 100 mL Teflon-lined autoclave and maintained at 160 °C for 12 h. After cooling, the solid was recovered by centrifugation (4000 rpm for 15 min), washed with absolute ethanol (4 x 20 mL) and dried at 70°C for 12 h.

2.5. Photocatalytic activity

The photocatalytic activities of BiOBr and rGO/BiOBr composites were evaluated in the degradation of the Orange II dye and of acetaminophen under visible light irradiation. All experiments were conducted at room temperature in a batch reactor equipped with a 400 nm cutoff filter. 30 mL of solution containing the catalyst and the pollutant (concentration of

10 mg/L for Orange II and 5 mg/L for acetaminophen) were magnetically stirred for 30 min in the dark to attain the adsorption-desorption equilibrium. For the degradation of Orange II, Sylvania LuxLine FHO T5 neon tubes were used as light source (light intensity at the surface of the Orange II solution = 8 mW/cm²). At given intervals, 2 mL of the solution were extracted and centrifuged (15000 rpm for 2 min) to remove the photocatalyst. The concentration of Orange II was determined by measuring the maximum absorbance at 485 nm using a UV-visible spectrometer. For the degradation of acetaminophen, a Hg/Xe lamp was used as light source (light intensity at the surface of the acetaminophen solution = 20 mW/cm²). The characteristic absorption peak of acetaminophen at 242 nm was used to determine the extent of photodegradation. Samples were also analyzed by HPLC using a Shimadzu model LC30 system (Shimadzu Corporation, Japan). 50 µL of sample were injected without column. The mobile phase consisted in water and acetonitrile in a 70/30 proportion (v/v) with 0.1 % formic acid (v/v). Samples were eluted at a flow rate of 0.2 mL/min. The UV signal was measured at 254 nm with a photometric diode array and using a cell with an optical path of 1 cm.

Reactive species produced during photocatalytic experiments were detected via *in situ* trapping experiments. p-Benzoquinone (BQ, O₂^{•-} radical scavenger), ammonium oxalate (AO, hole scavenger) and DMSO (electron scavenger) were added to the pollutant and photocatalyst solution before the adsorption-desorption phase. *Tert*-butanol (*t*-BuOH, •OH radical scavenger) was added to the solution before the irradiation phase. All scavengers were used at a 10 mM concentration except BQ that was used at a 0.1 mM concentration.

2.6. Characterization

Transmission electron microscopy (TEM) images were taken by placing a drop of the particles dispersed in water onto a carbon film-supported copper grid. Samples were studied using a Philips CM200 instrument operating at 200 kV. The X-ray powder diffraction (XRD) patterns were measured using Panalytical X'Pert Pro MPD diffractometer using Cu K α radiation. Thermogravimetric analysis was conducted under O₂ atmosphere from room temperature to 1000°C at a heating rate of 10°C/min using a TGA/DSC1 STAR equipment (Mettler-Toledo)

A Micromeritics Tristar II Plus Surface Characterization Analyzer instrument was used to measure the Brunauer-Emmet-Teller (BET) surface areas of the samples using liquid nitrogen (-196 °C). Prior to the analyses, the samples were out-gassed overnight under primary vacuum at 40°C on the ports of the Micromeritics VacPrep 061 degasser followed by 4 h out-gassing under primary vacuum on the analyse ports. The resulting isotherms were analysed using the BET method while the pore volume (V_{pore}) was determined using the total volume of nitrogen adsorbed at saturation.

All the optical measurements were performed at room temperature ($20 \pm 1^\circ\text{C}$) under ambient conditions. Absorption spectra of liquid samples were recorded on a Thermo Scientific Evolution 220 UV-visible spectrophotometer. The diffuse reflectance absorption spectra (DRS) were collected on a Shimadzu 2600-2700 UV-visible spectrophotometer. BaSO₄ powder was used as a standard for baseline measurements and spectra were recorded in a range of 250-750 nm. Photoluminescence emission spectra were measured on a Horiba Fluoromax-4 Jobin Yvon spectrofluorimeter.

The photoelectrochemical performance of as-prepared samples was measured in a three electrode cell with Pt wire as the counter electrode, a saturated Ag/AgCl electrode as reference electrode and FTO glass coated with BiOBr or rGO/BiOBr materials with a surface area of 1 cm² as the working electrode. 0.1 M Na₂SO₄ aqueous solution was used as electrolyte. The photocurrent densities were evaluated by measuring the current with and without 100 mW/cm² light illumination provided by a 300 W Xe arc lamp fitted with an AM 1.5G filter. The photocurrent response was recorded at a constant potential of + 0.30 V vs. the reference electrode by using a SP150 BioLogic potentiostat. Electrochemical impedance spectra (EIS) measurements were performed in the same workstation by applying a sinusoidal AC perturbation of 10 mV with a frequency range from 500 kHz to 0.01 Hz under open circuit potential conditions.

To identify intermediates produced during the degradation of acetaminophen, samples analyzed by HPLC were introduced in a Shimadzu MS2020 model mass spectrometer. Acquisition were done in ESI +/- mode, the scan was 50 to 500 uma in TIC conditions and three SIMS (152, 174 and 150 uma) measures were done simultaneously.

3. Results and discussion

3.1. Characterization of rGO/BiOBr photocatalysts

rGO/BiOBr composites were prepared by varying the loading in rGO (0.5, 1, 2.5 and 5 wt%) during the hydrothermal synthesis of BiOBr conducted at 160°C for 12 h. Thermogravimetric analysis (TGA) was used to get information about the thermal stability and to determine the rGO content in rGO/BiOBr composites (Fig. S1). The weak weight loss (< 0.5%) observed by heating until 150°C originates from the removal of water molecules adsorbed at the surface of the photocatalysts. Two apparent mass loss can be observed at higher temperatures for all materials. The first one occurring between 200 and 550°C originates from the decomposition of rGO, while the second one between 600 and 700°C can be attributed to the decomposition of BiOBr into Bi₂O₃. These results are in agreement with previous reports [31]. The first weight loss was used to determine the rGO content in rGO/BiOBr composites (Fig. S1b). For theoretical loadings in rGO of 0.5, 1, 2.5 and 5 wt%, the actual loadings were determined to be 0.29, 0.76, 1.32 and 1.78%, respectively.

The diffraction pattern of BiOBr shows intense and sharp signals which are indicative of its good crystallinity (Fig. 1a). These peaks can be indexed to a tetragonal phase with a space group of P4/nmn (129). The signals at 2θ values of 10.8, 21.9, 25.2, 31.7, 32.3, 32.7, 39.5, 46.2, 50.6 and 57.1° correspond to the (001), (002), (101), (102), (110), (003), (112), (004), (104) and (212) crystallographic planes of BiOBr (JCPDS Card No. 09-0393), respectively. The crystallinity of BiOBr was not affected after the association with rGO, indicating that rGO does not generate new crystal orientations of BiOBr. The typical diffraction peaks of rGO located at 2θ values values of 26 and 44.5° could not be detected in the rGO/BiOBr composites likely due to the low content in rGO and to their weak diffraction intensity compared to BiOBr.

The FT-IR spectrum of BiOBr shows a signal located at 500 cm⁻¹ corresponding to the Bi-O vibration and this peak is present in all rGO/BiOBr composites (Fig. 1b) [30]. Weak signals centered at 1721 and 1605 cm⁻¹ corresponding to the C=O vibration and to the skeletal vibration of rGO, respectively, can also be observed for the composites loaded with 2.5 and 5% rGO, indicating that GO was not fully reduced after the treatment with ascorbic acid followed by the hydrothermal process.

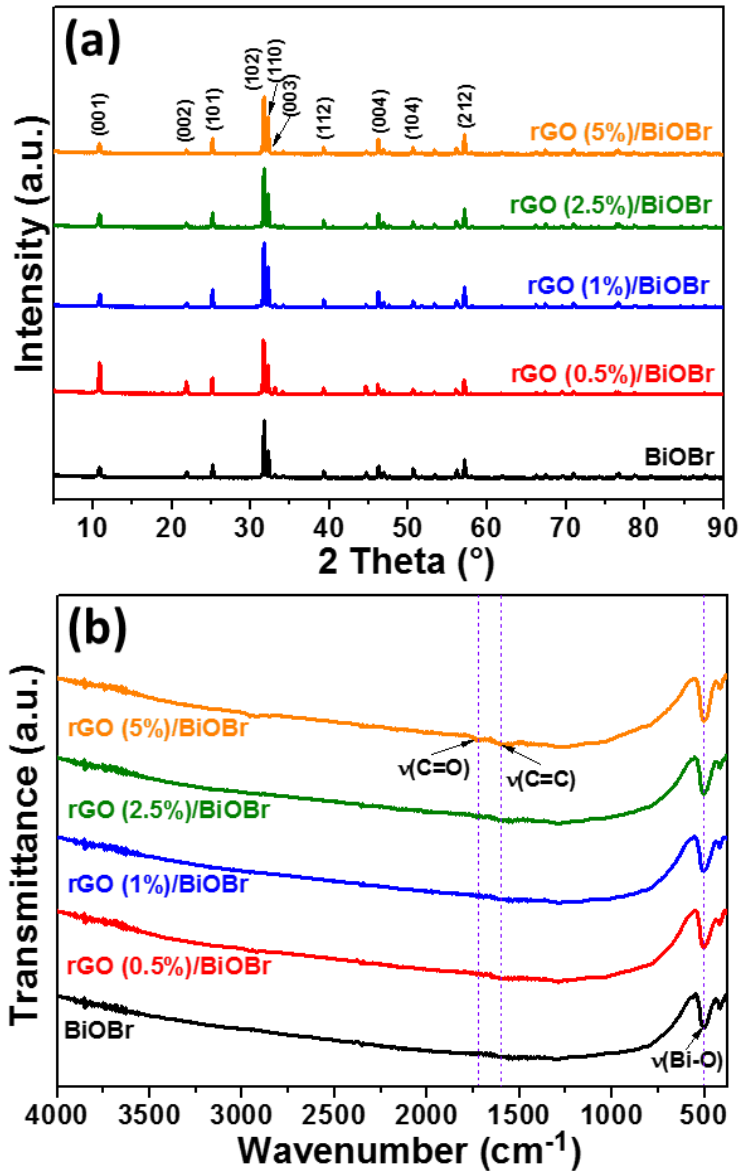


Fig. 1. (a) XRD patterns and (b) FT-IR spectra of BiOBr and rGO/BiOBr composites.

The Raman spectra of BiOBr and of BiOBr/rGO composites are shown in Fig. 2a. The signals observed at 103.2 and 149.9 cm⁻¹ correspond to the *A1g* internal Bi-Br stretching mode and to the *Eg* internal Bi-Br stretching mode, respectively [38,49]. The sharpness of these peaks further confirms the good crystallinity of BiOBr. The characteristic D (vibration of defects states in graphene sheets) and G (bond stretching of sp² carbon atoms) bands of rGO are located at 1343.1 and 1573.7 cm⁻¹, respectively, and can only be seen for the composites loaded with 2.5 and 5 wt% rGO (Fig. 2b). The intensity ratio of D and G bands (I_D/I_G) is of ca.

0.85, value indicative of the disorders in rGO (vacancies, grain boundaries and amorphous carbons).

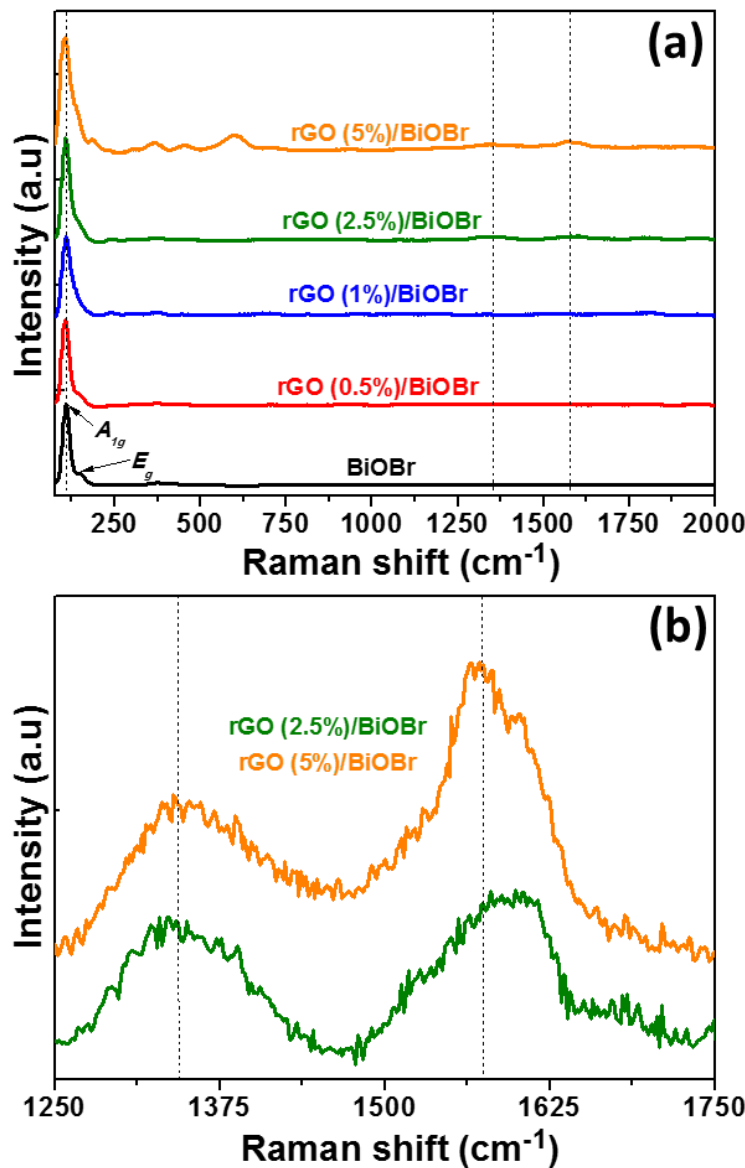


Fig. 2. (a) XRD Raman spectra of BiOBr and rGO/BiOBr composites and (b) magnification of the 1250-1750 cm⁻¹ region for rGO (2.5%) and rGO (5%)/BiOBr composites.

The morphology of BiOBr and of the rGO (1%)/BiOBr materials was characterized by SEM and TEM. SEM images show that BiOBr sheets have sizes varying between 2 and 15 µm and a thickness of ca. 400 nm (Fig. 3a-b). These sheets self-organize into flower-like microstructures with an average size of 35 µm to form 3D-porous networks with micrometer-sized pores. The SEM images also show that each flower-like assembly is

composed of randomly assembled BiOBr sheets. The assembly of BiOBr sheets is modified when their synthesis is conducted in the presence of rGO (Fig. 3 c-d). Although flower-like microstructures can still be observed, larger tubular assemblies of nanosheets with a length up to 100 μm are present in the rGO (1%)/BiOBr composite (Fig. 3c).

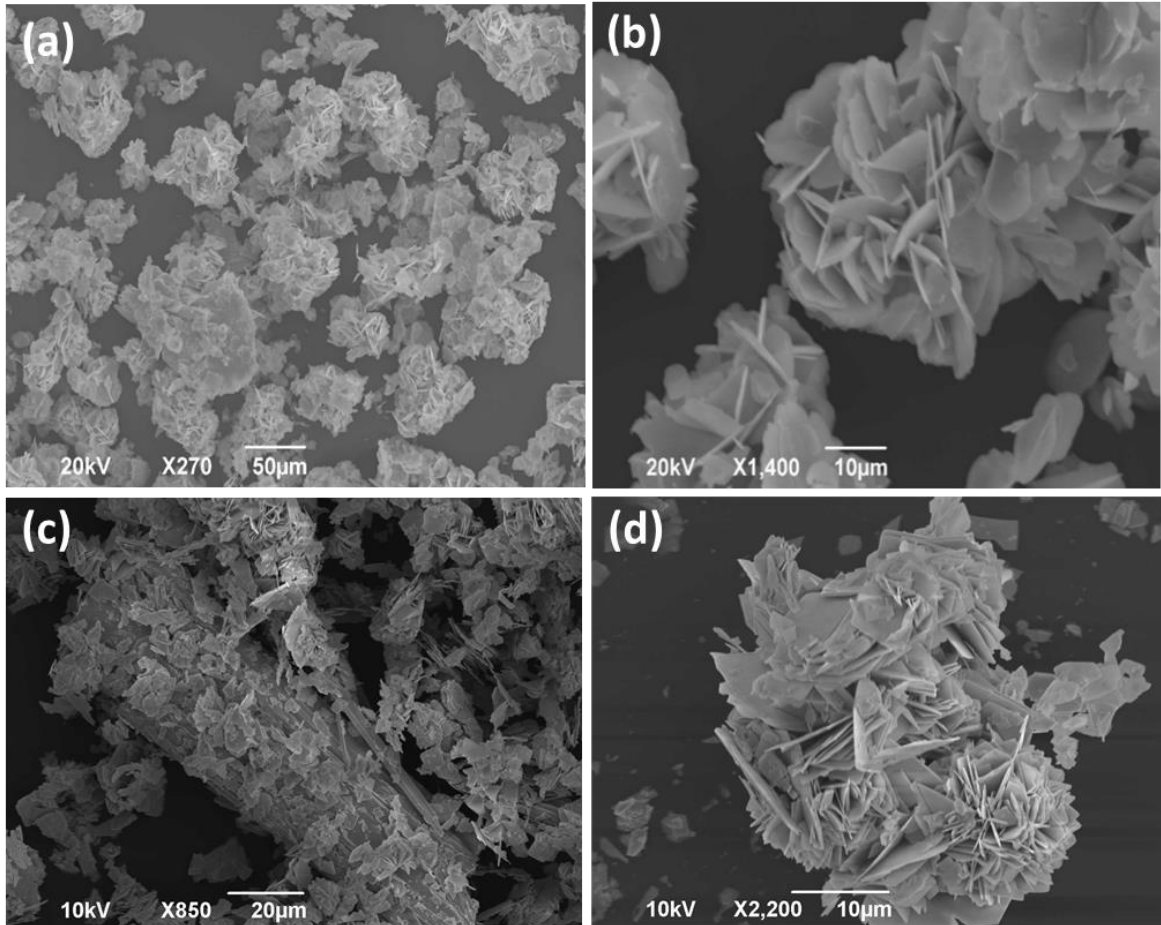


Fig. 3. SEM images of (a,b) BiOBr and (c,d) of the rGO (1%)/BiOBr composite.

The TEM images confirm the sheet-shaped structure of BiOBr and rGO/BiOBr composites (Fig. 4a-b). As shown in Fig. 4b, rGO deposits at the BiOBr sheets, indicating that a composite associating rGO and BiOBr with close contact was successfully prepared. The association of rGO and its relative uniform dispersion at the surface of BiOBr sheets was demonstrated by the energy dispersive X-ray spectroscopy (EDS) mapping (Fig. 5), in which a thin layer of C can be observed at the surface of BiOBr (Fig. 5e). This result is in accordance with our previous report showing that rGO deposits at the surface of nanocrystals during their solvothermal or hydrothermal synthesis [22,23]. An angle of 45° between the (200) and

(110) planes of BiOBr was also determined from the associated selected-area electron diffraction pattern (SAED) (inset of Fig. 4b), confirming that the favoured growth direction is along the [001] orientation. The HR-TEM image of the rGO (1%)/BiOBr sample shows continuous lattice fringes with an interplanar spacing of 0.27 nm corresponding to the (110) atomic plane of tetragonal BiOBr (d-spacing of 0.277 nm for the (110) reflection) (Fig. 4c). The fringes with spacing of 0.32 nm correspond to the (002) plane of rGO, which further confirms that rGO was successfully associated to BiOBr.

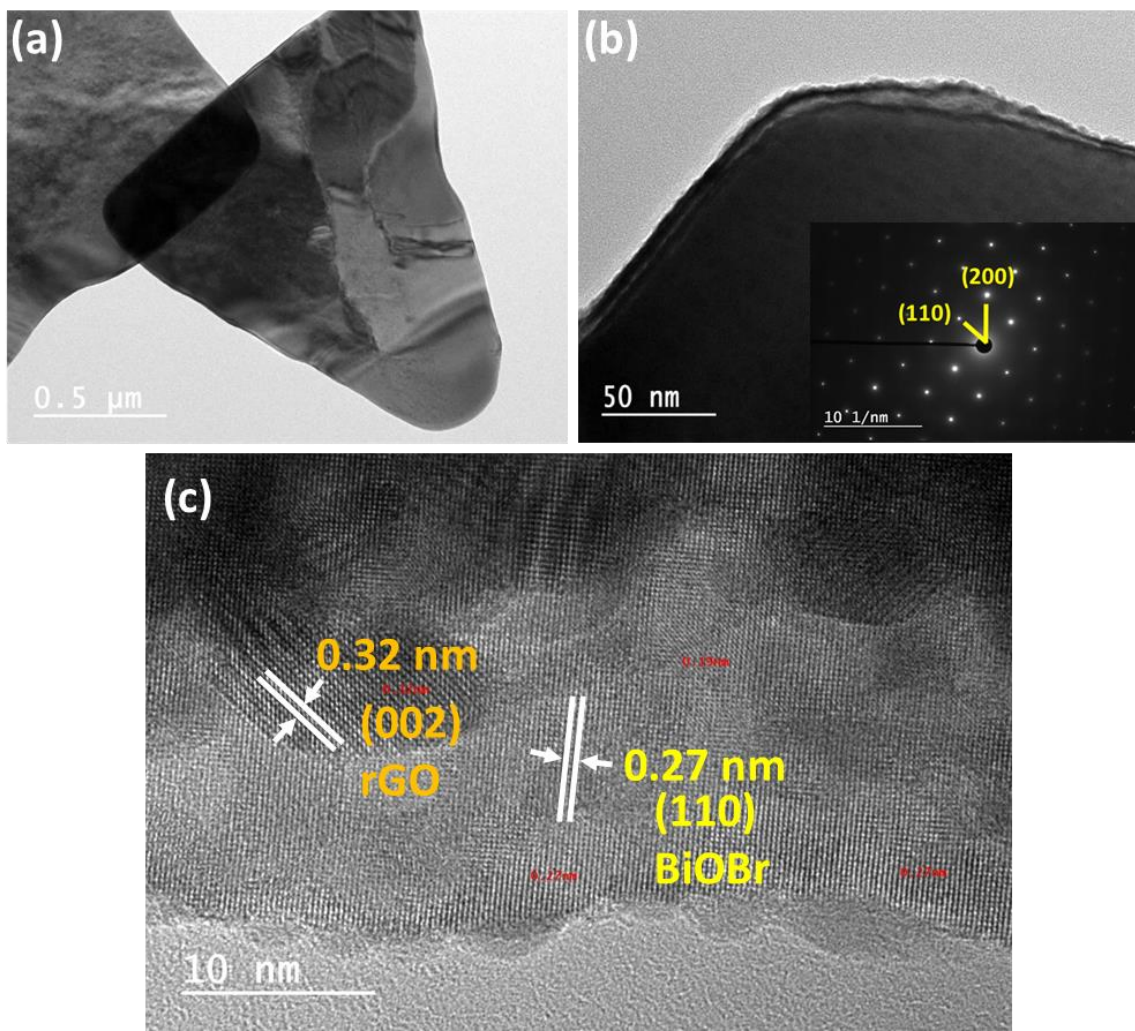


Fig. 4. (a-b) TEM and (c) HR-TEM images of the rGO (1%)/BiOBr composite. The inset of (b) shows the SAED pattern.

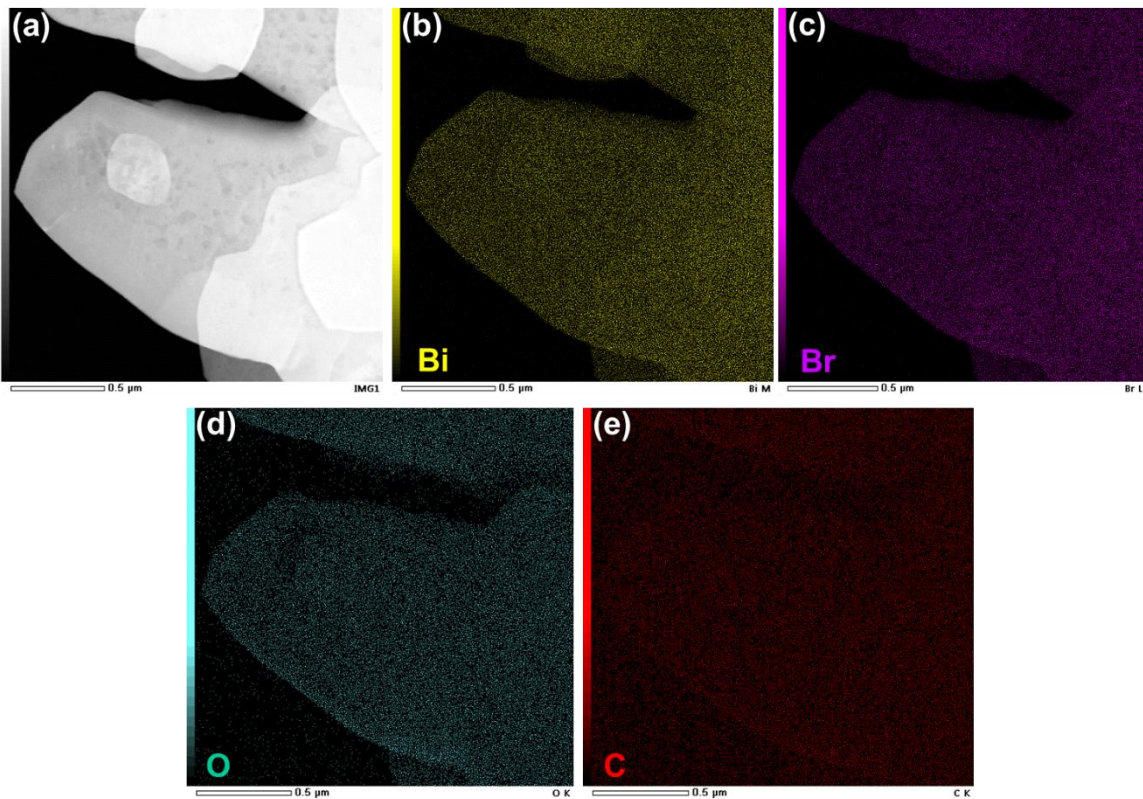


Fig. 5. (a) TEM image of the rGO (1%)/BiOBr composite, (b-e) EDX elemental mapping images of Bi, Br, O and C elements, respectively.

The surface element composition and the chemical state of elements present in the rGO (1%)/BiOBr composite were investigated by XPS (Fig. 6). The survey XPS spectrum shows that the sample is only composed of Bi, O, Br and C elements (Fig. S2). Two signals located at 160.17 and 165.48 eV corresponding to Bi 4f_{7/2} and Bi 4f_{5/2}, respectively, can be observed in the high resolution spectrum of Bi [30]. The splitting between these signals is of 5.31 eV, which confirms that Bi is present in the +3 oxidation state in the composite (Fig. 6a). The O 1s peak can be deconvoluted into two signals located at 530.78 and 533.18 eV, which can be attributed to O in BiOBr [37] and to O of C-O bonds in rGO [22], respectively (Fig. 6b). The Br 3d_{5/2} and Br 3d_{3/2} peaks appear at 69.10 and 70.12 eV, respectively (Fig. 6c). Finally, the C 1s signal can be deconvoluted into two peaks at 284.92 and 286.70 eV, corresponding to graphitic carbons and C-O bonds (alcohol, acid and epoxide functions) (Fig. 6d) [22,30]. These results further confirm that rGO/BiOBr composites were successfully synthesized via the hydrothermal method developed in the work.

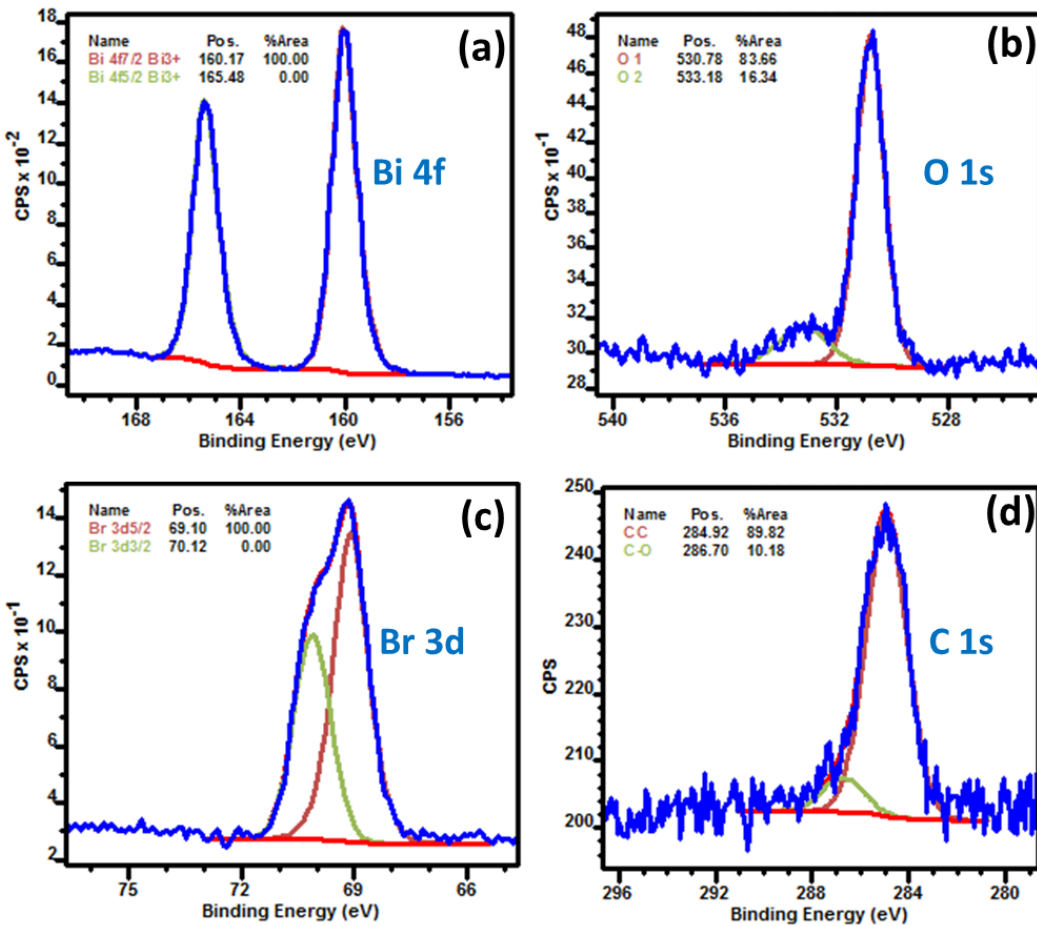


Fig. 6. High-resolution XPS spectra of Bi 4f, O 1s, Br 3d and C 1s for the rGO (1%)/BiOBr composite.

The UV-visible absorption spectra of BiOBr and of the rGO/BiOBr composites are shown in Fig. 7. rGO exhibits a dark grey color and a continuous absorption over the whole visible region. As can be seen, the association of BiOBr with rGO increases the visible light absorption likely due to the strong chemical bonds between these materials. The bandgaps of rGO/BiOBr composites were determined by plotting $(\alpha h\nu)^{1/2}$ vs $h\nu$ (where α is the absorption coefficient and $h\nu$ is the photon energy) and by extrapolating the linear part of the curves to the x axis (Fig. 7b). The bandgap of BiOBr is 2.70 eV, which is in accordance with previous reports [30,32]. Upon increasing the rGO content in the composites, a continuous decrease of the bandgap is observed (2.66, 2.60, 2.48 and 2.33 eV for composites loaded with 0.5, 1, 2.5 and 5% rGO, respectively), indicating a higher sensitivity of the composites to visible light which should be beneficial to the photocatalytic activity. The decrease of bandgap observed for rGO/BiOBr composites likely originates from the

formation of Bi-C bonds during the hydrothermal process via the bonding of some unpaired electrons on the surface of BiOBr, which is in accordance with previous reports [30].

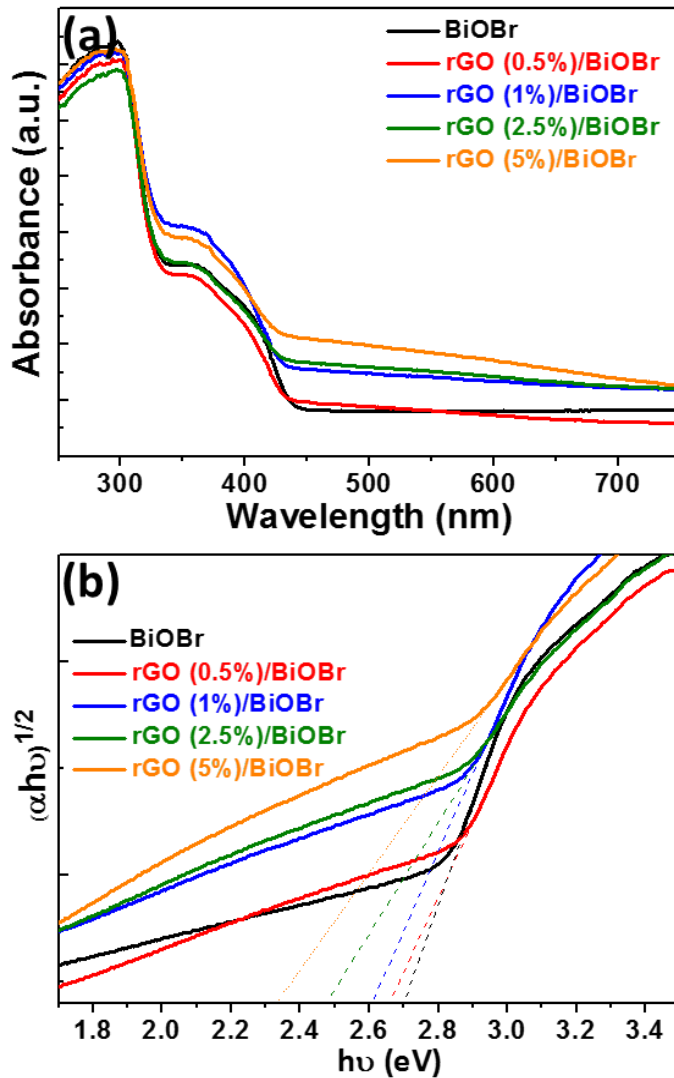


Fig. 7. (a) UV-vis absorption spectra of BiOBr and of rGO/BiOBr composites. (b) Plots of $(\alpha h\nu)^{1/2}$ vs $h\nu$ for the determination of the bandgaps of the photocatalysts.

3.2. Photocatalytic degradation of Orange II

The photocatalytic activity of BiOBr and rGO/BiOBr composites was first evaluated in the degradation of the Orange II dye under visible light irradiation (intensity of 8 mW/cm^2). A series of control experiments show that no bleaching of Orange II occurred in the absence of the photocatalyst or without light irradiation. After 30 min stirring in the dark to reach the

adsorption-desorption equilibrium (ca. 10% adsorption of the dye at the surface of the photocatalyst), light was turned on. The photocatalytic was found to depend on the rGO content in the composite and the highest activity towards the degradation of Orange II was observed for the rGO (1%)/BiOBr composite (Fig. 8a). The increase of the rGO loading (2.5 or 5%) was found to be detrimental on the photocatalytic activity likely due to the decrease of photocatalytically active BiOBr due to the deposition of rGO at its surface as previously shown by TEM. The time-dependent UV-vis absorption spectra of Orange II during its photodegradation with the rGO (1%)/BiOBr composite show a gradual decrease of the maximum absorption peak located at ca. 485 nm and the degradation efficiency reached 97% after 90 min irradiation. Meanwhile, the color of the dye solution changed from orange to transparent and no new absorption signals were observed, further indicating the effective degradation of Orange II.

The photodegradation of Orange II follows the pseudo-first-order model $\ln(C_0/C) = kt$, where C_0 and C are the concentrations of the dye at $t = 0$ and t , respectively, and k is the rate constant (Fig. S3). The rate constants determined for rGO/BiOBr with loadings in rGO of 0.5, 1, 2.5 and 5% are 0.029, 0.040, 0.024 and 0.028 min^{-1} , respectively. These values confirm that the rGO (1%)/BiOBr material is the most effective for the bleaching of Orange II.

Although dyes, amounts of catalysts used and light sources are not similar to those used in this work, the rGO (1%)/BiOBr favorably compares with graphene oxide-modified BiOBr photocatalysts described in the literature which allow between 75 and 100% dye bleaching after ca. 75-120 min visible light irradiation [29-46].

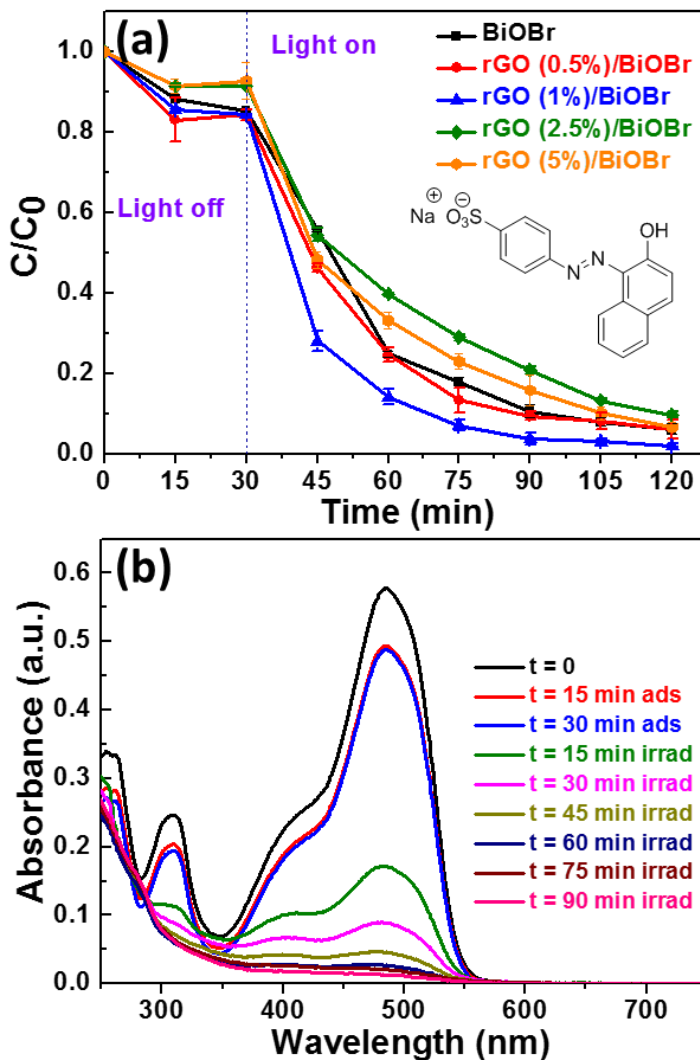


Fig. 8. (a) Photocatalytic performances of BiOBr and rGO/BiOBr composites for the degradation of Orange II under visible light irradiation (intensity of 8 mW/cm^2). (b) UV-vis absorption spectral changes during the photodegradation of Orange II with the rGO (1%)/BiOBr composite

3.3. Photocatalytic degradation of acetaminophen, catalyst stability and influence of pH

Pharmaceuticals are emerging pollutants that can be found as trace amounts among others in drinking water, groundwater, soils and sediments. Acetaminophen (ACT), also called paracetamol, is one of the most commonly used drug in the world due to its analgesic and antipyretic properties [50-52]. Between 58 and 68% of ACT is excreted from the body after ingestion [53]. Due to its modest biodegradability, ACT can be found at concentrations up to

65 µg/L in effluents. Moreover, ACT has been demonstrated to be toxic towards bacteria and plants [50-52].

The rGO (1%)/BiOBr was also found to be effective for the degradation of ACT as shown in Fig. 9a. After 105 min visible light irradiation, the removal efficiency of ACT is of 93% while it is only of 55% using pure BiOBr (Fig. 9b). The k values are 0.006 and 0.003 min⁻¹ for rGO (1%)/BiOBr and BiOBr, respectively (Fig. S4). After the photodegradation of ACT by the rGO (1%)/BiOBr catalyst, the total organic carbon (TOC) decreased by ca. 53% after 105 min of irradiation, further indicating that a great part of ACT was decomposed into CO₂ and H₂O. Recently, numerous photocatalysts like TiO₂, TiO₂/graphene, C-modified TiO₂ or Ti-Zr MOFs have been reported for the degradation of ACT under UV or simulated solar light irradiation [54-60]. The degradation efficiencies vary from 40 to 95% for irradiation times between 1 and 4 h. The photodegradation of ACT under visible light has been more rarely investigated. Catalysts like In₂S₃/Zn₂GeO₄ or Ag-, Pt- or Au-loaded TiO₂ that allow 95 and 100% degradation of ACT after 6 and 3 h irradiation, respectively, have recently been described [59,60]. Compared with these catalysts, the rGO (1%)/BiOBr photocatalyst exhibits a significantly higher activity (93% degradation in 105 min under visible light irradiation), indicating that the association of rGO with BiOBr promotes the generation of reactive species able to decompose ACT.

The stability of the rGO/BiOBr material for the degradation of ACT was evaluated by recycling the photocatalyst. After each run, the catalyst was recovered by centrifugation and reused without any treatment (Fig. 9c). No significant decrease of the photocatalytic activity was observed after the fifth reuse indicating that the rGO/BiOBr did not photocorrode during the repeated degradations of ACT, which further proves its high potential for water decontamination.

The pH of the aqueous solution is one key parameter influencing the photocatalytic activity since the charge of the catalyst and of the pollutant and thus their electrostatic interactions but also the positions of valence and of the conduction bands of the photocatalyst depend on pH [61,62]. The point of zero charge (pzc) of the rGO (1%)/BiOBr catalyst is of 5.11, value slightly higher to that pure BiOBr (4.81) (Fig. S5a). The pH of the ACT solution was adjusted using 0.1 M NaOH or HCl before conducting photocatalytic experiments and the results are depicted in Fig. S5b. At pH values below the pzc, a decrease of the photocatalytic activity efficiency of the rGO (1%)/BiOBr composite is observed (78 and 89% degradation at pH 2.5

and 4.5, respectively, after 105 min irradiation). The optimal degradation of ACT was observed at pH values ranging from 5.5 to 9.5, due to the association via hydrogen bonds between ACT and the negatively charged surface of the catalyst. The modest photocatalytic activity (60% degradation avec 105 min irradiation) observed at pH 11.5 likely originates from the repellency of the negatively charged ACT ($pK_{\text{phenol}} = 9.38$) with the negatively charged photocatalyst.

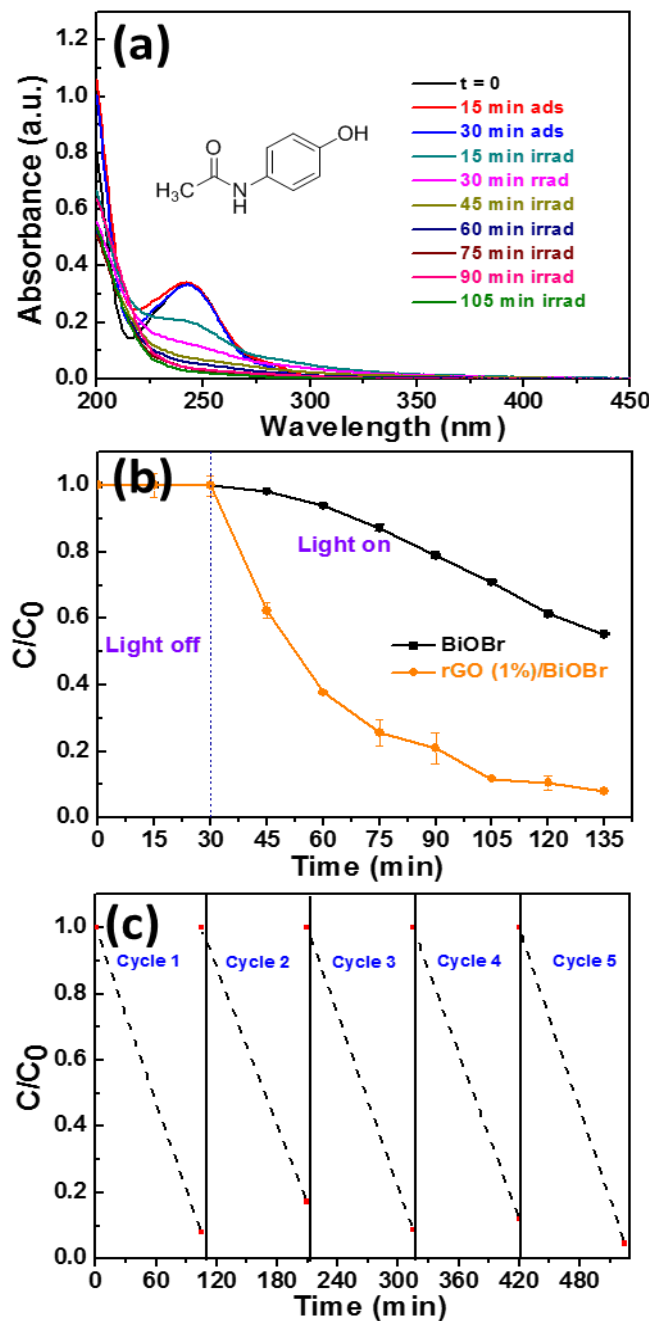


Fig. 9. (a) Temporal UV-vis absorption changes during the degradation of ACT under visible light irradiation (intensity of 20 mW/cm^2). (b) Photocatalytic degradation efficiencies of ACT

using BiOBr and rGO (1%)/BiOBr photocatalysts. (c) Recycling tests of the rGO (1%)/BiOBr catalyst for the degradation of ACT used at a concentration of 5 mg/L.

3.4. Mechanism

The specific surface area and the porosity of BiOBr and of rGO/BiOBr composites were characterized via N₂ adsorption-desorption isotherms and the results are given in Table 1. The isotherms are of type III according to the IUPAC classification, indicating the presence of mesopores (Fig. 10a). The first hysteresis loop observed in the lower relative pressure range ($0.4 < P/P_0 < 0.8$) is related to the pores originating from the association of BiOBr sheets into BiOBr nanoflowers while the second one observed at higher relative pressure ($0.9 < P/P_0 < 1$) is associated to the pores present between the secondary particles, which is in accordance with previous reports [63,64]. These results are consistent with the SEM images of BiOBr and rGO/BiOBr composites shown in Fig. 3.

Pure BiOBr exhibits a BET surface area of 7.38 m²/g. A significant increase of the BET surface area is observed for the rGO (0.5%)/BiOBr material (13.36 m²/g). Further increasing the loading in rGO from 1 to 5% induces a gradual decrease of the BET surface area (from 9.88 to 3.61 m²/g), likely originating from the deposition of rGO at the periphery of BiOBr sheets as shown by TEM analyses. The rGO (1%)/BiOBr material exhibits the highest photocatalytic activity but does not possess the highest BET surface area, which suggests that the BET surface area does not play a key role on the catalytic efficiency of the rGO/BiOBr samples. The Barrett-Joyner-Hallenda (BJH) method was used to determine the pore volumes (Fig. 10b). Results obtained show that the pore volume was not significantly affected by the loading with rGO but a continuous increase of the pore size was observed. The small pores with sizes varying from 7.52 to 11.11 nm are likely associated to the stacked nanosheets in BiOBr nanoassemblies.

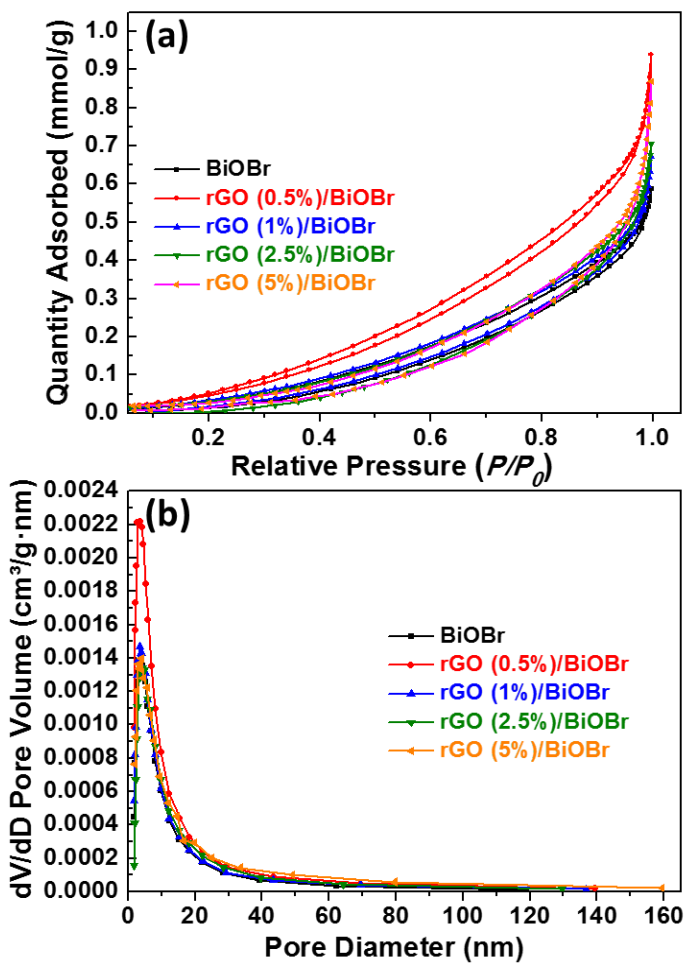


Fig. 10. (a) Nitrogen adsorption-desorption isotherms of BiOBr and rGO/BiOBr composites and (b) the corresponding pore size distributions.

Table 1. BET, pore volume, and pore size for BiOBr and rGO/BiOBr composites.

Sample	BET	Pore volume	Pore size
	(m^2/g)	(cm^3/g)	(nm)
BiOBr	7.38 ± 1.04	0.029	7.91
rGO (0.5%)/BiOBr	13.36 ± 1.93	0.030	7.52
rGO (1%)/BiOBr	9.88 ± 0.90	0.025	8.22
rGO (2.5%)/BiOBr	4.40 ± 0.67	0.022	9.93
rGO (5%)/BiOBr	3.61 ± 0.56	0.027	11.11

The photocatalytic efficiency also depends on the recombination rate of photogenerated electron/hole pairs. If the recombination is fast, less time is allowed to electrons and holes to react with oxygen and water molecules adsorbed at the surface of the catalyst and thus the production of the reactive species responsible for the photodegradation is decreased. The charge carrier separation and their lifetime were first investigated by photoluminescence (PL) spectroscopy (Fig. 11a). After excitation at 312 nm, pure BiOBr exhibits a broad PL ranging from 375 to 550 nm. After association with rGO, the shape of the PL signal is not altered but its intensity markedly decreased indicating that the electron/hole pair recombination in BiOBr is inhibited by the presence of rGO.

This was further evidenced by the transient photoelectrochemical (PEC) responses as these measurements correlate with the recombination efficiency of photogenerated charge carriers [62]. The photocurrent densities of rGO/BiOBr composites are in good accordance with their photocatalytic activities, the separation of electron-hole pairs being the most efficient in the rGO (1%)/BiOBr composite (Fig. 11b). Under visible light irradiation, the photocurrent measured for BiOBr deposited on FTO is of ca. 0.00085 mA. After association with 1 wt% rGO, the photocurrent increased to ca. 0.001 mA, indicating that the rGO (1%)/BiOBr composite more efficiently transfers the photogenerated charges to the working electrodes and thus that the separation of charge carriers is enhanced. Finally, the photocurrent quickly increases and remains almost stable when the light is turned on. A good reproducibility was also observed for all materials during the switching on and off cycles, indicating that the photoresponses are stable and reversible.

Electrochemical impedance spectroscopy was also used to get deep insight into the charge transport behavior in the absence of light excitation. All Nyquist plots exhibit semi-circle like curve and the diameters can be used to assess the impedance (Fig. 11c). The smallest semicircle is observed for the rGO (1%)/BiOBr sample, indicating that the association of BiOBr with 1% rGO can effectively reduce the charge transfer resistance at the material surface/interface. This result indicates a strongly improved electronic conductivity in the non-photoexcited state, which is beneficial for the charge separation during photocatalysis.

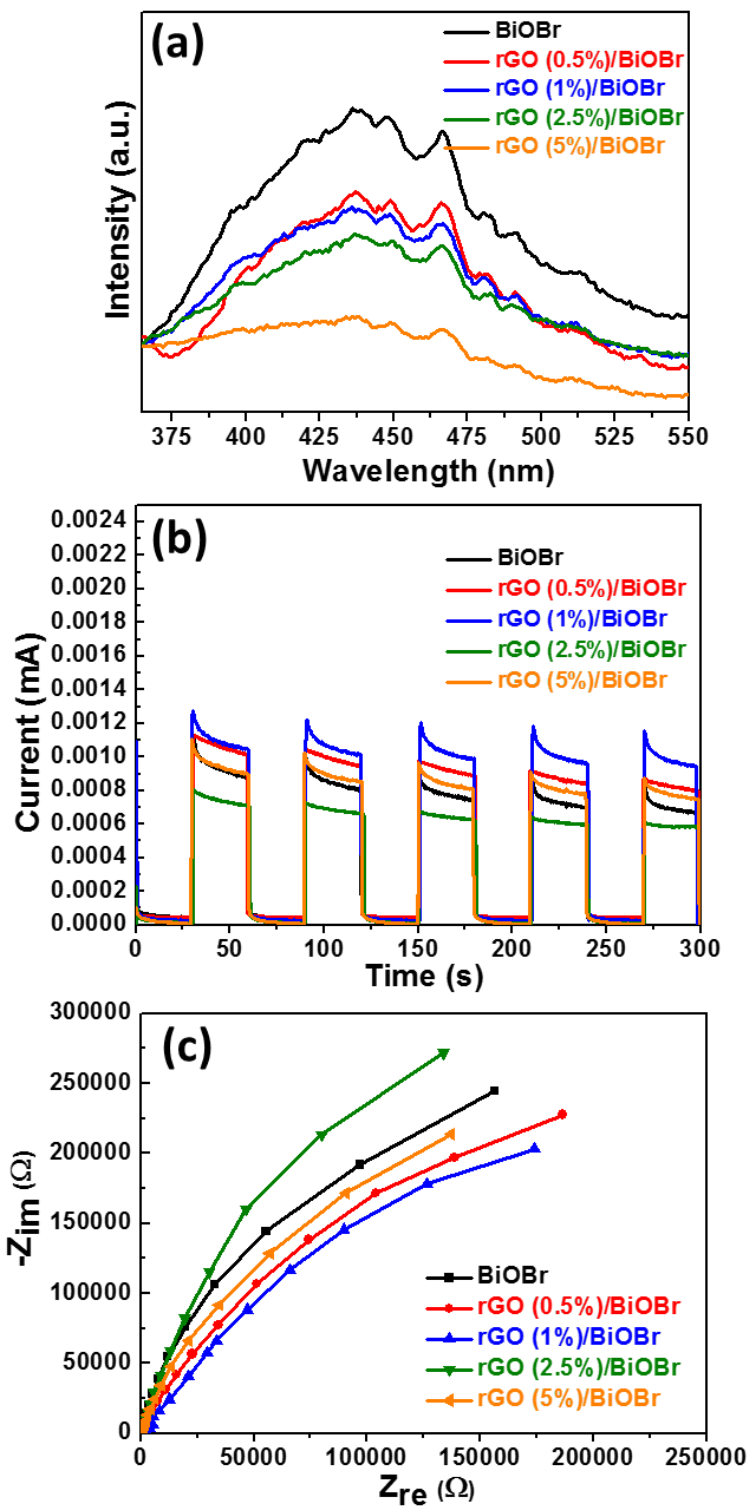


Fig. 11. (a) PL emission spectra, (b) transient photocurrent responses and (c) EIS Nyquist plots of BiOBr and rGO/BiOBr composites.

To determine the role played by the various reactive species generated during the photocatalytic process, different scavengers of these species were added during the degradation of ACT and the results are shown in Fig. 12a [22,23,62]. Tert-butanol (t-BuOH) used as hydroxyl \cdot OH radical scavenger and DMSO used as electron scavenger only weakly affect the photodegradation of ACT (87 and 93% degradation after 90 min irradiation, respectively), indicating that \cdot OH radicals and electrons only play a minor role in ACT removal. p-Benzoylquinone (BQ) used as $O_2^{\cdot-}$ radical scavenger and especially ammonium oxalate (AO) used as hole scavenger were found to be much more deleterious to the degradation of ACT (31 and 12% degradation after 90 min irradiation, respectively). These results demonstrate that $O_2^{\cdot-}$ radicals and holes play a key role in the photocatalytic process. The major role of $O_2^{\cdot-}$ radicals was further demonstrated by removing O_2 from the ACT solution by Ar bubbling before conducting the photodegradation of ACT (Fig. S5). In these experimental conditions, the degradation efficiency was reduced to 53%.

The electrochemical potentials of the valence band (VB) and of the conduction band (CB) of BiOBr are of high importance to understand the photodegradation mechanism over the rGO/BiOBr composite. E_{VB} was estimated according to the following equation :

$$E_{VB} = \chi - E^e + 0.5 E_g$$

where χ is the absolute electronegativity of BiOBr (6.176), E^e is the energy of free electrons on the hydrogen scale (ca. 4.5 eV) and E_g is the bandgap (2.60 eV for the rGO (1%)/BiOBr composite) [65]. The VB and CB edge potentials of BiOBr were estimated to be 2.976 and 0.376 eV vs NHE, respectively (Fig. 12b).

On the basis of the previously described experimental data, the photocatalytic mechanism can be explained as follows (Fig. 12c). Under visible light irradiation, the electrons in the VB of BiOBr are excited to the CB, leaving holes in the VB. Due to its p-type semiconductor nature, the Fermi energy level of BiOBr is located near the VB edge. The photogenerated electrons in the CB of BiOBr easily transfer to rGO due to the high working function of this material (0.08 eV vs NHE) and due to the internal electron field at the rGO/BiOBr interface [66]. The Schottky barrier at the interface of BiOBr and rGO inhibits the electron/hole recombination in BiOBr [67,68], as previously demonstrated by PL and PEC measurements. Due to the ability of rGO in storing and shuttling electrons, the electrons collected by rGO can react with oxygen molecules adsorbed at the surface of the photocatalyst to produce

O_2^\cdot . In the meantime, holes in the VB of BiOBr directly oxidize ACT into ACT^+ and, to a much lower extent, react with H_2O molecules to give HO^\cdot radicals.

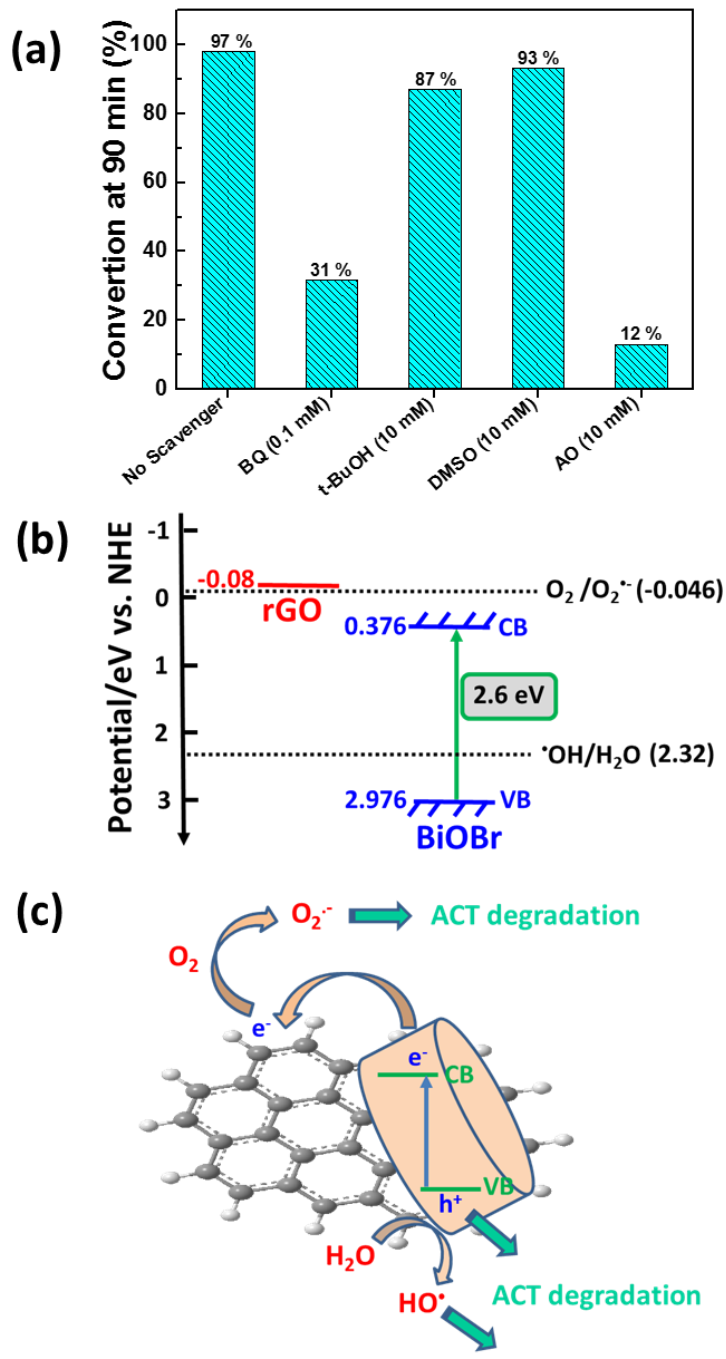


Fig. 12. (a) Influence of scavengers on the photodegradation of ACT using the rGO (1%)/BiOBr catalyst under visible light irradiation, (b) Schematic band structure of the rGO

(1%)/BiOBr catalyst, and (c) schematic illustration of the photocatalytic reaction process of the rGO/BiOBr catalyst.

3.5. Photodegradation intermediates of ACT

The intermediates formed during the photodegradation of ACT were identified by flow injection analysis-mass spectrometry (FIA-MS) in ESI mode. Among the products identified is hydroquinone ($m/z = 110$) which is likely formed via an *ipso*-substitution of the amide function by $O_2^{\cdot-}$ radicals generated during photocatalysis followed by the rupture of the hydroperoxyde bond (Fig. 13). Hydroxyquinol ($m/z = 126$) could also be detected as an intermediate, indicating a further hydroxylation of the aromatic ring (Fig. S7). Next, hydroquinone and hydroxyquinol are oxidized into mono- and dicarboxylic acids by cleavage of the aromatic ring. These results are in agreement with the photocatalytic pathways described in the literature for ACT [55,69].

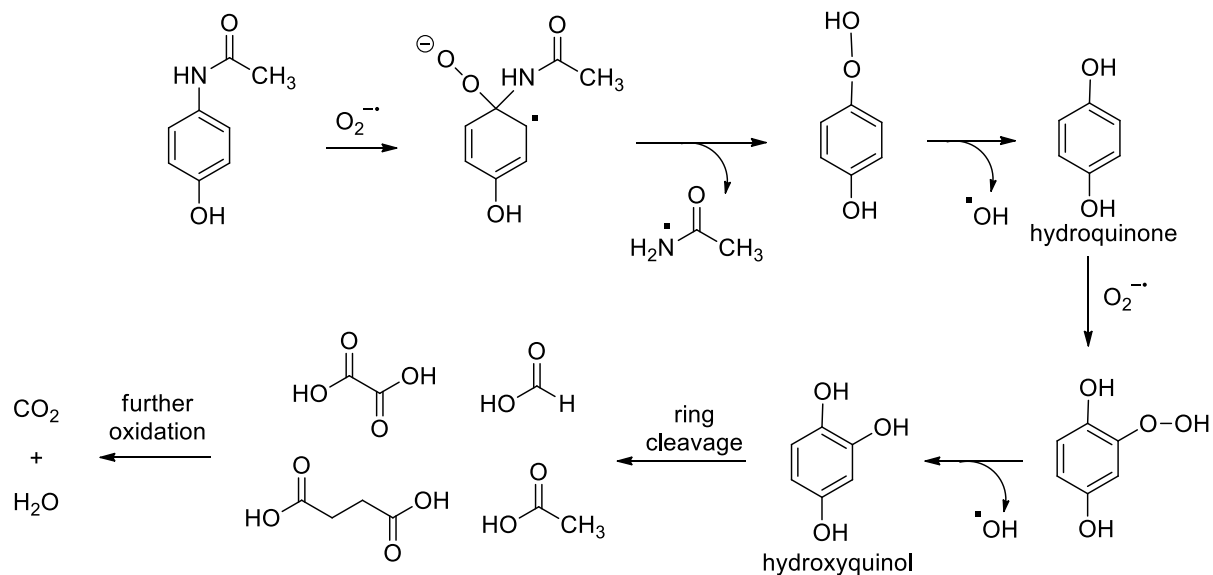


Fig. 13. Proposed degradation route of ACT mediated by the rGO (1%)/BiOBr photocatalyst.

4. Conclusion

In this paper, a hydrothermal method allowing the deposition of rGO at the surface of BiOBr sheets with exposed {001} facets was developed. The rGO (1%)/BiOBr composite exhibits high photocatalytic activity under visible light irradiation for the degradation of Orange II

and acetaminophen. On the basis of the characterization results, the enhanced photocatalytic activity of the rGO (1%)/BiOBr composite originates from the increased visible light absorption and from the effective charge separation and transportation due to the strong association of rGO with BiOBr sheets. This work highlights the potential of graphene-based materials for the design of heterostructured photocatalysts with high activity for environmental applications.

Acknowledgements

This work was supported partly by the french PIA project « Lorraine Université d'Excellence », reference ANR-15-IDEX-04-LUE. The authors thank Dr. Khalid Ferji and Steve Pontvianne for zeta potential measurements and TOC analyses, respectively.

Appendix A. Supplementary data

References

- [1] D.S. Bhatkhande, V.G. Pangarkar, A.A.C.M. Beenackers, Photocatalytic degradation for environmental applications – a review, *J. Chem. Technol. Biotechnol.* 77 (2002) 102-116.
- [2] S. Girish Kumar, L. Gomathi Devi, Review on modified TiO₂ photocatalysis under UV/Visible light: selected results and related mechanisms on interfacial charge carrier transfer dynamics, *J. Phys. Chem. A* 115 (2011) 13211-13241.
- [3] A. O. Ibhadon, P. Fitzpatrick, Heterogeneous photocatalysis: Recent advances and applications, *Catalysts* 3 (2013) 189-218.
- [4] J. Lia, N. Wu, Semiconductor-based photocatalysts and photoelectrochemical cells for solar fuel generation: a review, *Catal. Sci. Technol.* 5 (2015) 1360-1384.
- [5] J. Schneider, M. Matsuoka, M. Takeuchi, J. Zhang, Y Horiuchi, M. Anpo, D.W. Bahnemann, Understanding TiO₂ photocatalysis: mechanisms and materials, *Chem. Rev.* 114 (2014) 9919-9986.
- [6] C.B. Ong, L.Y. Ng, A. W. Mohammad, A review of ZnO nanoparticles as solar photocatalysts: Synthesis, mechanisms and applications, *Renew. Sust. Energ. Rev.* 81 (2018) 536-551.

- [7] M. Guan, C. Xiao, J. Zhang, S. Fan, Q. Cheng, J. Xie, M. Zhou, B. Ye, Y. Xie, Vacancy associates promoting solar-driven photocatalytic activity of ultrathin bismuth oxychloride nanosheets, *J. Am. Chem. Soc.* 135 (2013) 10411-10417.
- [8] M. Pan, H. Zhang, G. Gao, L. Liu, W. Chen, Facet-dependent catalytic activity of nanosheet-assembled bismuth oxyiodide microspheres in degradation of bisphenol A, *Environ. Sci. Technol.* 49 (2015) 6240-6248.
- [9] R. He, D. Xu, B. Cheng, J. Yu, W. Ho, Review on nanoscale Bi-based photocatalysts, *Nanoscale Horiz.* 3 (2018) 464-504.
- [10] H.F. Cheng, B.B. Huang, Y. Dai, Engineering BiOX (X = Cl, Br, I) nanostructures for highly efficient photocatalytic applications, *Nanoscale* 6 (2014) 2009-2026.
- [11] L. Ye, Y. Su, X. Jin, H. Xie, C. Zhang, Recent advances in BiOX (X = Cl, Br and I) photocatalysts: synthesis, modification, facet effects and mechanisms, *Environ. Sci.: Nano* 1 (2014) 90-112.
- [12] Q.Q. Du, W.P. Wang, Y.Z. Wu, G. Zhao, F.K. Ma, X.P. Hao, Novel carbon dots/BiOBr nanocomposites with enhanced UV and visible light driven photocatalytic activity, *RSC Adv.* 5 (2015) 31057-31063.
- [13] D. Zhang, J. Li, Q. Wang, Q. Wu, High {001} facets dominated BiOBr lamellas: facile hydrolysis preparation and selective visible-light photocatalytic activity, *J. Mater. Chem. A* 1 (2013) 8622-8629.
- [14] L. Li, L. Ai, C. Zhang, J. Jiang, Hierarchical {001}-faceted BiOBr microspheres as a novel biomimetic catalyst: dark catalysis towards colorimetric biosensing and pollutant degradation, *Nanoscale* 6 (2014) 4627-4634.
- [15] H. Li, J. Shang, Z. Ai, L. Zhang, Efficient visible light nitrogen fixation with BiOBr nanosheets of oxygen vacancies on the exposed {001} facets, *J. Am. Chem. Soc.* 137 (2015) 6393-6399.
- [16] D. Wu, L. Ye, H.Y. Yip, P. Keung Wong, Organic-free synthesis of {001} facet dominated BiOBr nanosheets for selective photoreduction of CO₂ to CO, *Catal. Sci. Technol.* 7 (2017) 265-271.
- [17] F. Cao, J. Wang, Y. Wang, J. Zhou, S. Li, G. Qin, W. Fan, An in situ Bi-decorated BiOBr photocatalyst for synchronously treating multiple antibiotics in water, *Nanoscale Adv.* 1 (2019) 1124-1129.

- [18] W. Fan, Q. Lai, Q. Zhang, Y. Wang, Nanocomposites of TiO₂ and reduced graphene oxide as efficient photocatalysts for hydrogen evolution, *J. Phys. Chem. C* 115 (2011) 10694-10701.
- [19] X. Liu, L. Pan, Q. Zhao, T. Lv, G. Zhu, T. Chen, T. Lu, Z. Sun, C. Sun, UV-assisted photocatalytic synthesis of ZnO-reduced graphene oxide composites with enhanced photocatalytic activity in reduction of Cr(VI), *Chem. Eng. J.* 183 (2012) 238-243.
- [20] J. Yu, J. Jin, B. Cheng, M. Jaroniec, A noble metal-free reduced graphene oxide-CdS nanorod composite for the enhanced visible-light photocatalytic reduction of CO₂ to solar fuel, *J. Mater. Chem. A* 2 (2014) 3407-3416.
- [21] C. Han, N. Zhang, Y.-J. Xu, Structural diversity of graphene materials and their multifarious roles in heterogeneous photocatalysis, *Nano Today* 11 (2016) 351-372.
- [22] H. Moussa, E. Girot, K. Mozet, H. Alem, G. Medjahdi, R. Schneider, ZnO rods/reduced graphene oxide composites prepared via a solvothermal reaction for efficient sunlight-driven photocatalysis, *Appl. Catal. B: Environ.* 185 (2016) 11-21.
- [23] B. Tatykayev, F. Donat, H. Alem, L. Balan, G. Medjahdi, B. Uralbekov, R Schneider, Synthesis of core/Shell ZnO/rGO nanoparticles by calcination of ZIF8/rGO composites and their photocatalytic activity, *ACS Omega* 2 (2017) 4946–4954.
- [24] D.A. Reddy, R. Ma, M.Y. Choi, T.K. Kim, Reduced graphene oxide wrapped ZnS–Ag₂S ternary composites synthesized via hydrothermal method: Applications in photocatalyst degradation of organic pollutants, *Appl. Surf. Sci.* 324 (2015) 725-735.
- [25] Q. Xiang, D. Lang, T. Shen, F. Liu, Graphene-modified nanosized Ag₃PO₄ photocatalysts for enhanced visible-light photocatalytic activity and stability, *Appl. Catal. B: Environ.* 162 (2015) 196-203.
- [26] D. Xu, L. Li, R. Ha, L. Qi, L. Zhang, B. Cheng, Noble metal-free RGO/TiO₂ composite nanofiber with enhanced photocatalytic H₂-production performance, *Appl. Surf. Sci.* 434 (2018) 620-625.
- [27] X. Li, R. Shen, S. Ma, X. Chen, J. Xie, Graphene-based heterojunction photocatalysts, *Appl. Surf. Sci.* 430 (2018) 53-107.
- [28] X. Li, J. Yu, S. Wageh, A.A. Al-Ghamdi, J. Xie, Graphene in Photocatalysis: A Review, *Small* 12 (2016) 6640-6696.
- [29] Z. Ai, W. Ho, S. Lee, Efficient visible light photocatalytic removal of NO with BiOBr-graphene nanocomposites, *J. Phys. Chem. C* 115 (2011) 25330-25337.

- [30] X. Tu, S. Luo, G. Chen, J. Li, One-pot synthesis, characterization, and enhanced photocatalytic activity of a BiOBr-graphene composite, *Chem. Eur. J.* 18 (2012) 14359-14366.
- [31] S. Song, W. Gao, X. Wang, X. Li, D. Liu, Y. Xing, H. Zhang, Microwave-assisted synthesis of BiOBr/graphene nanocomposites and their enhanced photocatalytic activity, *Dalton Trans.* 41 (2012) 10472-10476.
- [32] X. Zhang, X. Chang, M.A. Gondal, B. Zhang, Y. Liu, G. Ji, Synthesis and photocatalytic activity of graphene/BiOBr composites under visible light, *Appl. Surf. Sci.* 258 (2012) 7826-7832.
- [33] J.-Y. Liu, Y. Bai, P.-Y. Luo, P.-Q. Wang, One-pot synthesis of graphene-BiOBr nanosheets composite for enhanced photocatalytic generation of reactive oxygen species, *Catal. Commun.* 42 (2013) 58-61.
- [34] X.-X. Wei, C.-M. Chen, S.-Q. Guo, F. Guo, X.-M. Li, X.-X. Wang, H.-T. Cui, L.-F. Zhao, W. Li, Advanced visible-light-driven photocatalyst BiOBr-TiO₂-graphene composite with graphene as a nano-filler, *J. Mater. Chem. A* 2 (2014) 4667-4675.
- [35] W. Zhang, F. Dong, T. Xiong, Q. Zhang, Synthesis of BiOBr-graphene and BiOBr-graphene oxide nanocomposites with enhanced visible light photocatalytic performance, *Ceram. Int.* 40 (2014) 9003-9008.
- [36] S. Vadivel, M. Vanitha, A. Muthukrishnaraj, N. Balasubramanian, Graphene oxide–BiOBr composite material as highly efficient photocatalyst for degradation of methylene blue and rhodamine-B dyes, *J. Water. Process Eng.* 1 (2014) 17-26.
- [37] H. Liu, Y. Sun, Z. Chen, Z. Jin, Y. Wang, Graphene sheets grafted three-dimensional BiOBr_{0.2}I_{0.8} microspheres with excellent photocatalytic activity under visible light, *J. Hazard. Mater.* 266 (2014) 75-83.
- [38] Z. Yang, F. Cheng, X. Dong, F. Cui, Controllable in situ synthesis of BiOBr_xI_{1-x} solid solution on reduced graphene oxide with enhanced visible light photocatalytic performance, *RSC Adv.* 5 (2015) 68151-68158.
- [39] X. Li, C. Dong, K.-L. Wu, S.-H. Xia, Y. Hu, M. Ling, K. Liu, X.-L. Lu, Y. Ye, X.-W. Wei, Synthesis of nitrogen-doped graphene-BiOBr nanocomposites with enhanced visible light photocatalytic activity, *Mater. Lett.* 164 (2016) 502-504.
- [40] T. Jiang, J. Li, Z. Sun, X. Liu, T. Lu, L. Pan, Reduced graphene oxide as co-catalyst for enhanced visible light photocatalytic activity of BiOBr, *Ceram. Int.* 42 (2016) 16463-16468.

- [41] S.P. Patil, R.P. Patil, V.K. Mahajan, G.H. Sonawane, V.S. Shrivastava, S. Sonawane, Facile sonochemical synthesis of BiOBr-graphene oxide nanocomposite with enhanced photocatalytic activity for the degradation of Direct green, Mater. Sci. Semicond. Process. 52 (2016) 55-61.
- [42] J. S.; S. Rani K.S.; P. Ellappan, L.R. Miranda, Photodegradation of methylene blue using magnetically reduced graphene oxide bismuth oxybromide composite, J. Environ. Chem. Eng. 4 (2016) 534-541.
- [43] X. Yu, J. Shi, L. Feng, C. Li, L. Wang, A three-dimensional BiOBr/RGO heterostructural aerogel with enhanced and selective photocatalytic properties under visible light, Appl. Surf. Sci. 396 (2017) 1775-1782.
- [44] A.M. Alansi, M. Al-Qunaibit, I.O. Alade, T.F. Qahtan, T. A. Saleh, Visible-light responsive BiOBr nanoparticles loaded on reduced graphene oxide for photocatalytic degradation of dye, J. Mol. Liq. 253 (2018) 297-304.
- [45] X. Yu, J. Shi, L. Feng, C. Li, L. Wang, A three-dimensional BiOBr/RGO heterostructural aerogel with enhanced and selective photocatalytic properties under visible light, Appl. Surf. Sci. 396 (2017) 1775-1782.
- [46] Y. Bao, K. Chen, Novel Z-scheme BiOBr/reduced graphene oxide/protonated g-C₃N₄ photocatalyst: Synthesis, characterization, visible light photocatalytic activity and mechanism, Appl. Surf. Sci. 437 (2018) 51-61.
- [47] K. Wang, J. Ruan, H. Song, J. Zhang, Y. Wo, S. Guo, D. Cui, Biocompatibility of graphene oxide, Nanoscale Res. Lett. 6 (2011) 8.
- [48] J. Zhang, H. Yang, G. Shen, P. Cheng, J. Zhang, S. Guo, Reduction of grapheme oxide via L-ascorbic acid, Chem. Commun. 46 (2010) 1112-1114.
- [49] J.E.D. Davies, Solid state vibrational spectroscopy—III[1] The infrared and raman spectra of the bismuth(III) oxide halides, J. Inorg. Nucl. Chem. 35 (1973) 1531-1534.
- [50] M.J.N. Gotootos, C.-C. Su, M.D.G. De Luna, M.-C. Lu, Kinetic study of acetaminophen degradation by visible light photocatalysis, J. Environ. Sci. Heal. A 49 (2014) 892-899.
- [51] C.-T. Chang, J.-J. Wang, T. Ouyang, Q. Zhang, Y.-H. Jing, Photocatalytic degradation of acetaminophen in aqueous solutions by TiO₂/ZSM-5 zeolite with low energy irradiation, Mater. Sci. Eng. B 196 (2015) 53-60.
- [52] G. Fan, H. Peng, J. Zhang, X. Zheng, G. Zhu, S. wang, L. Hong, Degradation of acetaminophen in aqueous solution under visible light irradiation by Bi-modified titanate

nanomaterials: morphology effect, kinetics and mechanism, *Catal. Sci. Technol.* 8 (2018) 5906-5919.

[53] N. Muir, J.D. Nichols, J.M. Clifford, J. Sykes, Comparative bioavailability of aspirin and paracetamol following single dose administration of soluble and plain tablets, *Curr. Med. Res. Opin.* 13 (1997) 491-500.

[54] C.J. Lin, W.-T. Yang, C.-Y. Chou, S.Y. Hsuan Liou, Hollow mesoporous TiO₂ microspheres for enhanced photocatalytic degradation of acetaminophen in water, *Chemosphere* 152 (2016) 490-495.

[55] H. Tao, X. Liang, Q. Zhang, C.-T. Chang, Enhanced photoactivity of graphene/titanium dioxide nanotubesfor removal of Acetaminophen, *Appl. Surf. Sci.* 324 (2015) 258-264.

[56] P. Xiong, J. Hu, Decomposition of acetaminophen (Ace) using TiO₂/UVA/LED system, *Catal. Today* 282 (2017) 48-56.

[57] A. Gomez-Aviles, M. Penas-Garzon, J. Bedia, J.J. Rodriguez, C. Belver, C-modified TiO₂ using lignin as carbon precursor for the solar photocatalytic degradation of acetaminophen, *Chem. Engineer. J.* 358 (2019) 1574-1582.

[58] A. Gomez-Aviles, M. Penas-Garzon, J. Bedia, D.D. Dionysiou, J.J. Rodriguez, C. Belver, Mixed Ti-Zr metal-organic-frameworks for the photodegradation of acetaminophen under solar irradiation, *Appl. Catal. B: Environ.* 253 (2019) 253-262.

[59] O. Nasr, O. Mohamed, A.-S. Al-Shirbini, A.-M. Abdel-Wahab, Photocatalytic degradation of acetaminophen over Ag, Au and Pt loaded TiO₂ using solar light, *J. Photochem. Photobiol. A: Chem.* 374 (2019) 185-193.

[60] T. Yan, T. Wu, Y. Zhang, M. Sun, X. Wang, Q. Wei, B. Du, Fabrication of In₂S₃/Zn₂GeO₄ composite photocatalyst for degradation of acetaminophen under visible light, *J. Colloid Interface Sci.* 506 (2017) 197-206.

[61] C.-H. Chiou, C.-Y. Wu, R.-S. Juang, Influence of operating parameters on photocatalytic degradation of phenol in UV/TiO₂ process, *Chem. Eng. J.* 139 (2008) 322-329.

[62] H. Moussa, B. Chouchene, T. Gries, L. Balan, K. Mozet, G. Medjahdi, R. Schneider, Growth of ZnO nanorods on graphitic carbon nitride gCN sheets for the preparation of photocatalysts with high visible-light activity, *ChemCatChem* 10 (2018) 4987-4997.

[63] Z. Jia, F. Wang, F. Xin, B. Zhang, Simple solvothermal routes to synthesize 3D BiOBr_xI_{1-x} microspheres and their visible-light-induced photocatalytic properties, *Ind. Eng. Chem. Res.* 50 (2011) 6688-6694.

- [64] J. Yu, S. Liu, H. Yu, Microstructures and photoactivity of mesoporous anatase hollow microspheres fabricated by fluoride-mediated self-transformation, *J. Catal.* 249 (2007) 59-66.
- [65] Y. Xu, M. A. A. Schoonen, The absolute energy positions of conduction and valence bands of selected semiconducting minerals, *Am. Mineral.* 85 (2000) 543-556.
- [66] M. Zhu, Y. Dong, B. Xiao, Y. Du, P. Yang, X. Wang, Enhanced photocatalytic hydrogen evolution performance based on Ru-trisdicarboxybipyridine-reduced graphene oxide hybrid, *J. Mater. Chem.* 22 (2012) 23773-23779.
- [67] Y.S. Chen, J.C. Crittenden, S. Hackney, L. Sutter, D.W. Hand, Preparation of a novel TiO₂-based p-n junction nanotube photocatalyst, *Environ. Sci. technol.* 2005, 39, 1201-1208.
- [68] Z. Ai, W. Ho, S. Lee, Efficient visible light photocatalytic removal of NO with BiOBr-graphene nanocomposites, *J. Phys. Chem. C* 2011, 115, 25330-25337.
- [69] E. Moctezuma, E. Leyva, C.A. Aguilar, R.A. Luna, C. Montalvo, Photocatalytic degradation of paracetamol: Intermedites and total reaction mechanism, *J. Hazard. Mater.* 243 (2012) 130-138.